ADVANCED MATERIALS
www.advmat.de

Exceptionally High Saturation Magnetic Flux Density and Ultralow Coercivity via an Amorphous–Nanocrystalline Transitional Microstructure in an FeCo-Based Alloy

Xuesong Li, Jing Zhou, Laiquan Shen, Baoan Sun, Haiyang Bai,* and Weihua Wang*

High saturation magnetic flux density (B_s) of soft magnetic materials is essential for increasing the power density of modern magnetic devices and motor machines. Yet, increasing B_s is always at the expense of high coercivity (H_c), presenting a general trade-off in the soft magnetic material family. Here, superior comprehensive soft magnetic properties, i.e., an exceptionally high B_s of up to 1.94 T and H_c as low as 4.3 A m^{-1} are unprecedentedly combined in an FeCo-based alloy. This alloy is obtained through a composition design strategy to construct a transitional microstructure between amorphous and traditional nanocrystalline alloys, with nanocrystals (with < 5 nm-sized crystal-like regions around) sparsely dispersed in an amorphous matrix. Such transitional microstructure possesses extremely low magnetic anisotropy caused by the annihilation of quasi-dislocation dipoles, and a strong magnetic exchange interaction, which leads to excellent comprehensive magnetic properties. The results provide useful guidelines for the development of the next generation of soft magnetic materials, which are promising for applications of high-frequency, high-efficiency, and energy-saving devices.

1. Introduction

Soft magnetic materials are responsible for the energy generation and conversion in various electromagnetic devices and motor power machines and are essential in the electrified world. In the view of global energy crisis and the stringent requirements of emission reduction, modern electronics (such as motors and generators) are developing toward high frequency, miniaturization, and high efficiency.[1,2] Consequently, there is a pressing need to develop new soft magnetic materials with superior comprehensive properties, such as a combination of high saturation magnetic flux density (B_s, for reducing the device volume and increasing the power density), low coercivity (H_c), and low magnetostriction (highly desirable in high-frequency applications).[3–5] Silicon steels are the most commonly used soft magnetic materials at present, yet they suffer from high core loss and low energy conversion efficiency.[6] Especially at high frequency, the core loss of silicon steels will increase exponentially, leading to serious heating problems of devices.[7] Fe-based amorphous alloys are a new class of soft magnetic materials with great potential developed in recent decades.[8] Arising from the unique disordered structure, Fe-based amorphous alloys exhibit much lower H_c and higher resistivity than that of silicon steels, resulting in a much lower core loss. Thermal treatment on these alloys can induce nanocrystals in the amorphous matrix, which may further reduce energy loss.[9] However, the B_s of amorphous/nanocrystalline (AN) alloys are much lower than that of silicon steels (1.9–2.0 T), e.g., the maximum B_s of commercial AN alloys are only ≈1.63 T (METGLAS2605),[10] which has become the main drawback to their applications in high-power-density scenarios.

Enduring efforts have been made to improve the B_s of AN alloys over the past decades.[8] One of the most commonly used methods is to increase the content of ferromagnetic elements in these soft magnetic alloys.[11] Based on the strategy, some amorphous and nanocrystalline alloys with high B_s have been successfully developed in Fe-metalloid and Fe-metalloid-Cu alloy systems which usually contain a small number of metalloids elements and ultrahigh content of ferromagnetic elements.[12,13] However, as the content of ferromagnetic elements increases, the glass forming ability (GFA) of these alloys rapidly decreases, which makes the nanocrystallization process harsh and uncontrollable. As a result, it is difficult to obtain a low H_c through simple and efficient thermal treatment processing, leading to an inversion relationship between B_s and

X. Li, J. Zhou, L. Shen, B. Sun, H. Bai, W. Wang
Institute of Physics
Chinese Academy of Sciences
Beijing 100190, China
E-mail: sunba@iphy.ac.cn; hybai@iphy.ac.cn
X. Li, J. Zhou, B. Sun, H. Bai, W. Wang
Songshan Lake Materials Laboratory
Dongguan 523808, China
X. Li, W. Wang
School of Energy Power and Mechanical Engineering
North China Electric Power University
Beijing 102206, China
J. Zhou, W. Wang
School of Mechanical Engineering
Dongguan University of Technology
Dongguan 523808, China
The ORCID identification number(s) for the author(s) of this article can be found under https://doi.org/10.1002/adma.202205863.

DOI: 10.1002/adma.202205863

H_c. The poor thermal stability and harsh nucleation-growth processes in these high-B_s AN alloys make this design strategy based on increasing the content of ferromagnetic elements approach the limit in breaking the trade-off of high B_s and low H_c. For example, the recently developed $Fe_{85.5}B_{10}Si_2P_2C_{0.5}$ AN alloy exhibits super-high B_s of 1.87 T but high H_c of 12 A m^{-1}, and such high B_s can only be obtained under the condition of rapid annealing.[11] How to overcome the trade-off between the B_s and H_c presents a major challenge in the AN soft magnetic alloys.

It is well known that the amorphous state after thermal annealing in Fe-based alloys could achieve a low H_c due to the low magnetic anisotropy,[14] while the precipitation of soft magnetic crystalline phases through the nanocrystallization process can improve the B_s.[15] Inspired by this, some transition state between the fully amorphous structure and nanocrystalline structure seems to be able to unite the high B_s with the low H_c. In this work, we proposed an innovative composition design concept that enables us to construct a unique microstructure of nanocrystals sparsely dispersed in the amorphous matrix. Such microstructure exhibits the combination of extremely low magnetic anisotropy caused by the annihilation of quasi-dislocation dipole and a strong magnetic exchange interaction.[16–18] Consequently, such design strategy enables us to develop a new amorphous/nanocrystalline transition (ANT) alloy with a unique microstructure, possessing a combination of exceptionally high B_s, ultralow H_c, and other excellent soft magnetic properties, which is promising for modern electronics with high power density and high efficiency.

2. Compositional Design Strategy

According to the discussion above, an ANT alloy with a microstructure of nanocrystals sparsely dispersed in an amorphous matrix is promising for reaching a subtle balance between the high B_s and the low H_c. To achieve this goal, we use the following composition design strategy: suitable ratio of ferromagnetic elements (such as Fe, Co et al.) is chosen to maximize the local magnetic moment amplitude and maintain the GFA,[19,20] and meanwhile some micro-alloying elements shall be added to form controllable nanocrystalline structure.[21] First, we select Fe–B binary amorphous alloy as the basic alloy system. As the lightest metalloid element, the addition of B not only can effectively improve the GFA, but also has the weakest effect on the proportion of ferromagnetic elements as compared with other metalloid elements. However, excessive amounts of B lead to the precipitation of Fe–B compounds during the nanocrystallization process, deteriorating the soft magnetic properties.[22,23] Therefore, we substitute the B with a small amount of Si, improving the combination of GFA and magnetic softness for its intersolubility with bcc-Fe to form bcc-(Fe, Si).[24] Moreover, the vacancies in 3*d* atomic orbitals of ferromagnetic atoms are contributed for the local magnetic moment amplitude, and these vacancies will be filled up by outer shell electrons of metalloid element in ferromagnetic-based alloys.[25] Therefore, an appropriate ratio of Si to B elements maximizes the amplitude of the local magnetic moment. Second, according to the Slater–Pauling curves,[26] gradual substitution of Co for Fe causes the magnetic exchange interaction to increase initially and then decrease (**Figure 1**), and there is a critical proportion of Fe to Co

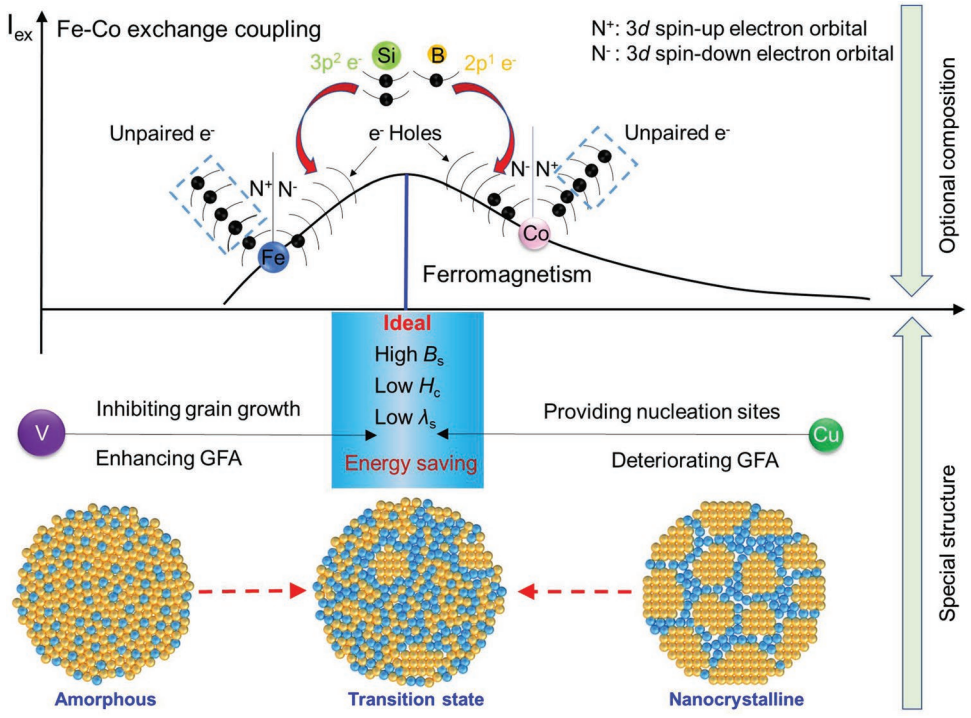

Figure 1. Sketches of alloy design strategy. A suitable ratio of ferromagnetic elements (e.g., Fe, Co) is chosen to maximize the local magnetic moment amplitude and maintain the GFA, and meanwhile, some micro-alloying elements (e.g., Cu, V et al.) shall be added to form controllable nanocrystalline structure.

with the strongest magnetic exchange interaction. The scenario has been verified in Fe-based amorphous and nanocrystalline alloys previously reported.[12,27–30] Therefore, an optimum proportion of Fe to Co should be determined to achieve the strongest magnetic exchange interaction in Fe-based AN alloys. Finally, in order to form a controllable nanocrystalline structure, the nucleation-promoting element of Cu and diffusion-inhibiting element of V are added to control the formation, nucleation, and growth of the nanocrystals.[1,9] Since Cu and V elements have opposite effects on the GFA of amorphous precursors, it is necessary to control their total content and the ratio between them.[31]

3. Microstructure and Thermal Properties

According to the above design concept, a series of FeCoBSiVCu amorphous alloys were developed by laboriously optimizing the composition. The XRD patterns of partial alloy compositions (with the ferromagnetic element content ≈85–87%) (Figure S1, Supporting Information) were used to identify the amorphous structure. As shown in the figure, the variation tendency of GFA and manufacturability of FeCoBSiVCu alloys validate the effectiveness of the alloy design concept. With the increase of Co and V content, the thickness of amorphous ribbons improves to 26 and 30 μm, respectively, indicating the enhancement of GFA. However, an increase of the Cu and total ferromagnetic elements decreases the GFA, which can be confirmed by the observation of obvious crystallization peak for $(Fe_{0.8}Co_{0.2})_{85}B_{12}Si_{0.5}V_{0.5}Cu_{1.5}$ and $(Fe_{0.8}Co_{0.2})_{87}B_{12}Si_2V_{0.5}Cu_{0.5}$ ribbons with thickness of 17 μm.

According to the results above, we selected the $(Fe_{0.8}Co_{0.2})_{85}B_{12}Si_2V_{0.5}Cu_{0.5}$ (denoted as $(Fe_{0.8}Co_{0.2})_{85}$) alloy with relatively high content of ferromagnetic elements and high GFA. The thermal properties and microstructure of the alloy were further investigated. The melt-spun ribbons with a thickness of 26 um of the $(Fe_{0.8}Co_{0.2})_{85}$ alloy exhibit a fully amorphous structure, which can be verified by typical maze-like patterns in the image of the transmission electron microscope (TEM) (Figure S2, Supporting Information). Differential scanning calorimetry (DSC) measurements of the alloy ribbon show a two-stage crystallization behavior (Figure S3, Supporting Information), with the first crystallization peak (T_{x1} = 655 K) and second crystallization peak (T_{x2} = 805 K). The two crystallization stages correspond to the precipitation of α-Fe (Co, Si) and Fe_2B phases, respectively, according to the previous reported results.[19] It is worth mentioning that the $(Fe_{0.8}Co_{0.2})_{85}$ amorphous alloy shows a large ΔT_x (= $T_{x2} - T_{x1}$) exceeding 150 K, which is much larger than other Fe-based amorphous alloys and is a benefit for keeping the low cost of manufacturability and good compositional adjustability.[11,32]

Based on the DSC result, a proper magnetic-field-assisted (MFA) heat treatment was conducted to modulate its microstructure. After 10 min of longitudinal MFA heat treatment, $(Fe_{0.8}Co_{0.2})_{85}$ ANT alloy exhibits a unique microstructure of dot-like nanocrystalline grains sparsely distributed in the amorphous matrix, according to the TEM images shown in **Figure 2**a,b. The selected-area electron diffraction (SAED) pattern (the inset of Figure 2a) confirms that these nanocrystals

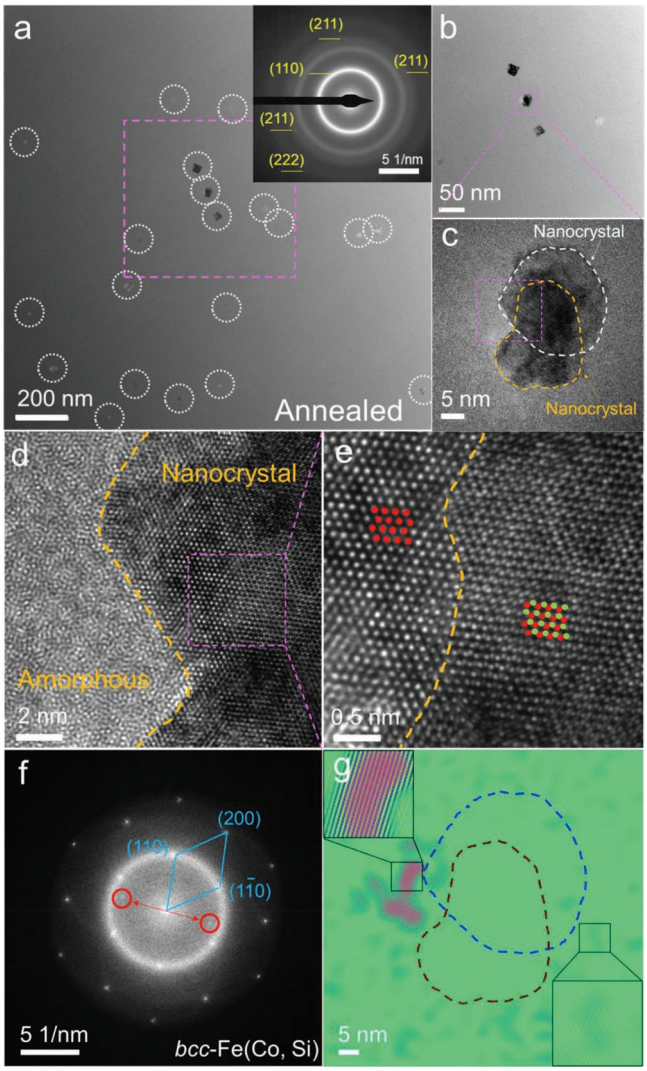

Figure 2. Microstructure of $(Fe_{0.8}Co_{0.2})_{85}$ ANT alloy with nested nanocrystals together with <5 nm-sized CLRs dispersed in an amorphous matrix. a) TEM image of annealed sample with 10 min of longitudinal MFA heat treatment at 673 K, showing the microstructure of dot-like nanocrystalline grains sparsely distributed in amorphous matrix. The inset shows an SAED pattern, indicating a bcc structure of the nanocrystals. b) Enlarged image of the pink square area in (a). c) High-resolution TEM image of the pink square area in (b). d) High-resolution TEM image of the pink square area in (c), showing a distinct interface between amorphous and nanocrystal. e) High-resolution TEM image of the pink square area in (d), showing two groups of crystal lattice arrangements (marked by red and green polka dot patterns, respectively) in the overlap of two grains. f) FFT pattern of (c). g) IFFT pattern of extra spots in (f) (pointed by red circles), showing the existence of CLRs in the amorphous matrix around the grains.

are bcc-Fe (Co, Si) phases. The volume fraction of nanocrystals in the amorphous matrix is very small (≈0.5%), which is much lower than that (≈80%) of typical Fe-based nanocrystalline alloys obtained via a thermal treatment of amorphous precursors.[9] After statistical analysis of the grain size in the figure, it can be seen that the nanocrystalline grains have small grain sizes ranging from 10 to 25 nm, but they do not exhibit a

very regularly round shape, as compared to previously reported high-B_s Fe-based nanocrystalline alloys.[11,32]

The high-resolution TEM image (Figure 2c) of a selected particle of $(Fe_{0.8}Co_{0.2})_{85}$ ANT alloy (marked by pink rectangle in Figure 2b) indicates that the irregular grain shape is due to the superposition of two approximately elliptical grains in space, which are marked by white and yellow dotted curves, respectively. For more clarity, Figure 2d,e shows the progressively magnified areas as marked by the pink rectangles in Figure 2c,d, respectively. It can be seen that the nanocrystals have a sharp interface with the amorphous matrix, and two groups of crystal lattice arrangements (indicated by red and green polka dot patterns, respectively) can be observed in the overlap of two grains. Figure 2f is the fast Fourier transform (FFT) pattern of Figure 2c, which also confirms bcc-Fe(Co, Si) structure of the precipitated grains. Interestingly, a group of spots (circled in red), weaker in intensity than sharp spots from bcc spots, can also be observed. It indicates the existence of some kind of a medium-range order (MRO).[33] As we know, the iconic diffraction for short-range order (SRO) is the diffuse scattering in the form of large-sized disks. Here, the counterpart by MRO becomes spots. This radical change to occur in reciprocal space is ascribed to an increase in sizes of MRO entities as compared to that of SRO, thus, allowing the presence of sharp diffraction spots to reflect the periodicity of ordering structures.[34,35] Furthermore, a high-resolution lattice image-based analysis was carried out through the inverse fast Fourier transform (IFFT) from the FFT patterns. The corresponding IFFT image of the extra spots (Figure 2g) obviously shows that some crystal-like regions (CLRs, composed of severe MRO structures) exist in the amorphous matrix around the grains, and the vast majority of CLRs are of 1–5 nm in size and uniformly distributed, except that some regions tend to clump together near the overlapping grains. Based on the results above, it can be concluded that a unique microstructure of nested nanocrystals together with <5 nm-sized CLRs dispersed in an amorphous matrix has been obtained in $(Fe_{0.8}Co_{0.2})_{85}$ ANT alloy.

4. Excellent Magnetic Properties

Figure 3a shows the hysteresis loops of melt-spun amorphous ribbons: $Fe_{85}B_{12}Si_2V_{0.5}Cu_{0.5}$ (denoted as Fe_{85}), $(Fe_{0.9}Co_{0.1})_{85}B_{12}Si_2V_{0.5}Cu_{0.5}$ (denoted as $(Fe_{0.9}Co_{0.1})_{85}$), $(Fe_{0.8}Co_{0.2})_{85}$, and $(Fe_{0.8}Co_{0.2})_{86}B_{11}Si_2V_{0.5}Cu_{0.5}$ (denoted as $(Fe_{0.8}Co_{0.2})_{86}$), and the inset shows the values of B_s varying with the compositions. It is clearly seen that the B_s first increase from 1.58 to 1.84 T with the increase of Co addition from 0 to 17 at%, and then decrease to 1.72 T with the further increase of the total content of ferromagnetic elements to 86 at%. As we know, the B_s generally increase with the increase of the total content of ferromagnetic elements. However, it is also reported that excessive content of ferromagnetic elements leads to a higher coordination number and a lower interatomic distance,

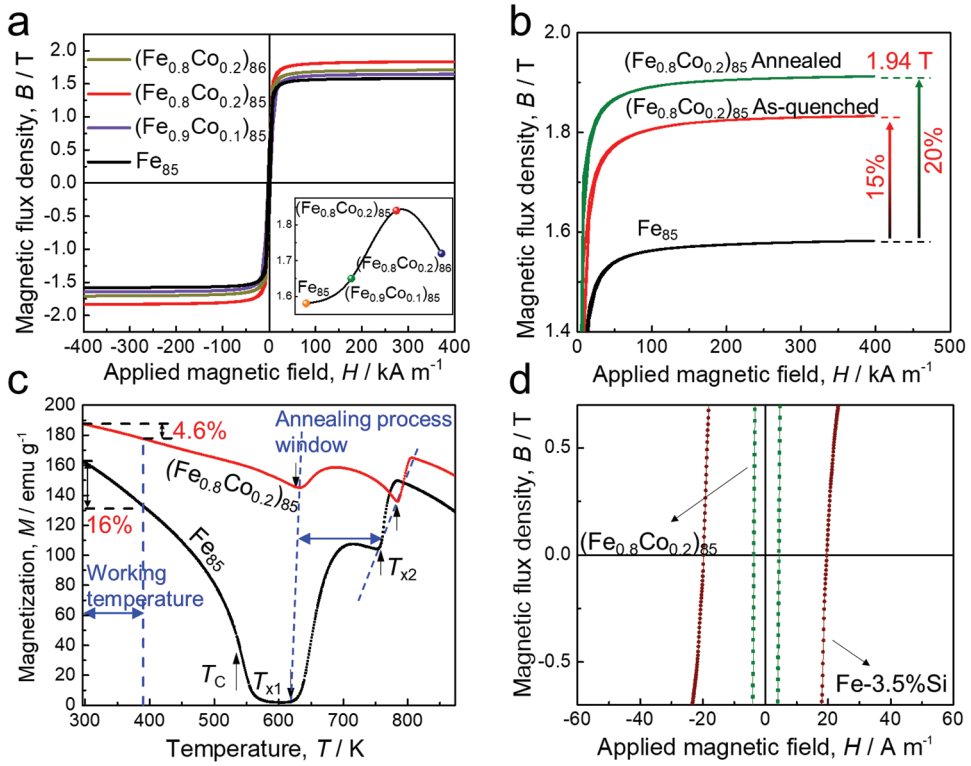

Figure 3. Magnetic properties of $(Fe_{0.8}Co_{0.2})_{85}$ alloy and other compared soft magnetic materials. a) Hysteresis loops of melt-spun Fe_{85}, $(Fe_{0.9}Co_{0.1})_{85}$, $(Fe_{0.8}Co_{0.2})_{85}$, and $(Fe_{0.8}Co_{0.2})_{86}$ alloy ribbons. The inset is the variation of B_s values with different compositions. b) Saturated magnetization curves of Fe_{85}, as-quenched $(Fe_{0.8}Co_{0.2})_{85}$, and annealed $(Fe_{0.8}Co_{0.2})_{85}$ alloy ribbons. c) Thermal-magnetization curves of as-quenched Fe_{85} and $(Fe_{0.8}Co_{0.2})_{85}$ alloys, showing the magnetization decrease at working temperature and increase in the range of annealing process window. d) amplified *B*–*H* loops of annealed $(Fe_{0.8}Co_{0.2})_{85}$ alloy and Fe–3.5%Si alloy.

which will reduce the amplitude of local magnetic moment, thereby decreasing B_s.[19,20] Therefore, the $(Fe_{0.8}Co_{0.2})_{85}$ alloy with the proper proportion of ferromagnetic elements shows the highest value of B_s among all the amorphous alloys. This is another reason that we select $(Fe_{0.8}Co_{0.2})_{85}$ alloy as the studying sample mentioned above.

Actually, in order to obtain the unique microstructure of sparsely dispersed nanocrystals in an amorphous matrix, we conducted a longitudinal-magnetic-field-assisted annealing at 673 K with the annealing time (t_a) ranging from 5 to 15 mins for exploring the optimal parameters. For very short t_a, the $(Fe_{0.8}Co_{0.2})_{85}$ alloy remains in a fully amorphous state after annealing. While with the long t_a (15 min), there are a large number of grains formed in the amorphous matrix, and these grains rapidly grow in size, presenting an irregular polygon shape (Figure S4, Supporting Information). The variation of microstructure results in a large difference in soft magnetic properties. Figure S5 (Supporting Information) shows the changes in B_s, H_c, and effective permeability (μ_e) at the frequency of 1 kHz with annealing time ranging from 5 to 15 min at 673 K for the $(Fe_{0.8}Co_{0.2})_{85}$ alloy. It can be seen that the B_s increase with elevated annealing time with exceptional high B_s for t_a above 10 min. Meanwhile, the H_c decreases gradually from 8.4 to 4.3 A m^{-1} with the increasing t_a, and then increases to 12.5 A m^{-1} with further increasing t_a to 15 min. In addition, the μ_e shows an opposite t_a dependence, that is, first increases to the maximum value of 8046 within 10 min, then rapidly decreases to 398 with t_a of 15 min. It is worth noting that the magnified hysteresis loops in Figure 3b show that the B_s of $(Fe_{0.8}Co_{0.2})_{85}$ alloy can reach 1.94 T after annealing for 10 min, exhibiting the improvement of 20% and 5% as compared to the annealed Fe_{85} and as-cast $(Fe_{0.8}Co_{0.2})_{85}$ alloy, respectively. Figure 3c shows the temperature dependence of magnetization (M) of Fe_{85} and $(Fe_{0.8}Co_{0.2})_{85}$ alloys, respectively. As can be seen, the Fe_{85} alloy exhibits a low value of T_C (543 K), and a drastically decreasing rate (16%) of M from room temperature to 393 K, which is detrimental for the device application at high-load conditions. For the $(Fe_{0.8}Co_{0.2})_{85}$ alloy, the M remains almost unchanged in the wide temperature range before crystallization, and the decreasing rate of M at 393 K (an international standard) reduces to 4.6% as compared with Fe_{85} alloy. Furthermore, the $(Fe_{0.8}Co_{0.2})_{85}$ alloy at this temperature range is still in a strong ferromagnetic state, suggesting the strong influences of the spontaneous magnetic field on the multi-mode relaxation and cluster processes, further indicating that the T_C for $(Fe_{0.8}Co_{0.2})_{85}$ alloy is higher than its T_{x1} value (655 K).[36] Such a high T_C of $(Fe_{0.8}Co_{0.2})_{85}$ also benefits the stability of soft magnetic properties operating at high temperatures. This alloy also exhibits a low H_c of 4.3 A m^{-1}, which is only one-fifth of that of Fe-3.5%Si alloy (Figure 3d). Based on these results, we can conclude that, by modulating the microstructure through magnetic-field-assisted annealing, a novel $(Fe_{0.8}Co_{0.2})_{85}$ ANT alloy has been developed, and exhibits superior comprehensive magnetic properties, e.g., exceptional high B_s of 1.94 T and low H_c of 4.3 A m^{-1}.

The extremely high B_s exceeding 1.9 T for the $(Fe_{0.8}Co_{0.2})_{85}$ alloy after annealing is presumed to originate from the combination of the following factors: (1) With the suitable substitution of Co for Fe, the enhanced exchange coupling of Fe–Co leads to the maximum values of the local magnetic moment amplitude and atomic volume.[19] In addition, it can also promote electron transfer into the spin-up 3*d* band of the Fe atom, which enlarges the unpaired electron concentration. (2) The suitable ratio between ferromagnetic metals (Fe, Co) and nonmetallic atoms (B, Si) suppresses the p–d electron interaction, hence increasing the number of 3d electron holes that are the source of the magnetic moment.[20] (3) The B_s of AN alloy are determined by the residual amorphous phase and precipitated phase: $B_s = B_{sc}V_{cry} + B_{sa}(1 - V_{cry})$, where B_{sc} and B_{sa} are the saturation flux density of crystalline phase and amorphous phase, respectively, V_{cry} is the crystallization volume fraction. With magnetic field-assisted annealing, some nested nanocrystals precipitated in the amorphous matrix (Figure 2c), which contributes to the further enhancement of B_s for $(Fe_{0.8}Co_{0.2})_{85}$ ANT alloy. In addition, the formation of CLRs indicates the development of a higher level of Fe-Fe (Co) pairs with preferred orientation along the direction of the external field, resulting in enhanced exchange interactions among Fe-Fe (Co) pairs and improved B_s.[37–39]

To highlight the exceptional high B_s of $(Fe_{0.8}Co_{0.2})_{85}$ ANT alloy, we collected the existing data of Fe-based nanocrystalline alloys (FINEMET-type, NANOPERM-type, HITPERM-type, Fe-(BSiPC)-Cu-type, Fe-(BSiPC)-type) and typical silicon steels previously reported,[9,11,19,27–31,40–56] and present these data with the mass fraction of ferromagnetic elements (**Figure 4**a). Normally, increasing ferromagnetic element content results in higher B_s and inferior GFA. However, we found that the high ferromagnetic element content approaching the formation limit of amorphous alloys leads to a downward trend of B_s. This may be due to the fact that the excessive content of ferromagnetic elements leads to the higher coordination number and the lower interatomic distance, which both decrease the amplitude of local magnetic moment and hence reduce B_s. Intriguingly, $(Fe_{0.8}Co_{0.2})_{85}$ ANT alloy is right at the threshold of ferromagnetic content reaching the maximum B_s of 1.94 T (comparable to the limit value of Si-steels). Meanwhile, the mass fraction of ferromagnetic element for the alloy is only 95.18%, which exhibits a relatively higher GFA than that of other high-B_s nanocrystalline alloys.

The values of B_s and H_c for $(Fe_{0.8}Co_{0.2})_{85}$ ANT alloy (marked by red star) and other nanocrystalline alloys (FINEMET-type, NANOPERM-type, HITPERM, other Cu-free, and other Cu-doped) previously reported were collected and compared in Figure 4b.[9,11,19,27–31,40–56] As can be seen, the increment of B_s is usually accompanied by the deterioration of H_c, presenting a trade-off relationship. Here, the $(Fe_{0.8}Co_{0.2})_{85}$ ANT alloy developed by our design strategy has the combination of an exceptionally high B_s up to 1.94 T that surpass almost all AN alloys and a low H_c of 4.3 A m^{-1} comparable to FINEMET-type alloys, challenging the B_s–H_c trade-off relationship. To evaluate the annealing processing ability of the alloy, we also summarized the relationship between T_{x1} and ΔT_x among nanocrystalline alloys with the B_s higher than 1.6 T (Figure 4c).[11,27–30,40–47] As can be seen, the $(Fe_{0.8}Co_{0.2})_{85}$ ANT alloy combines large ΔT_x (150 K) and low T_{x1} (655 K) among these alloys, indicating the low temperature required for nanocrystallization process and wide annealing process window. These features facilitate the control of nanocrystalline structure during the crystallization process, as well as practical applications.

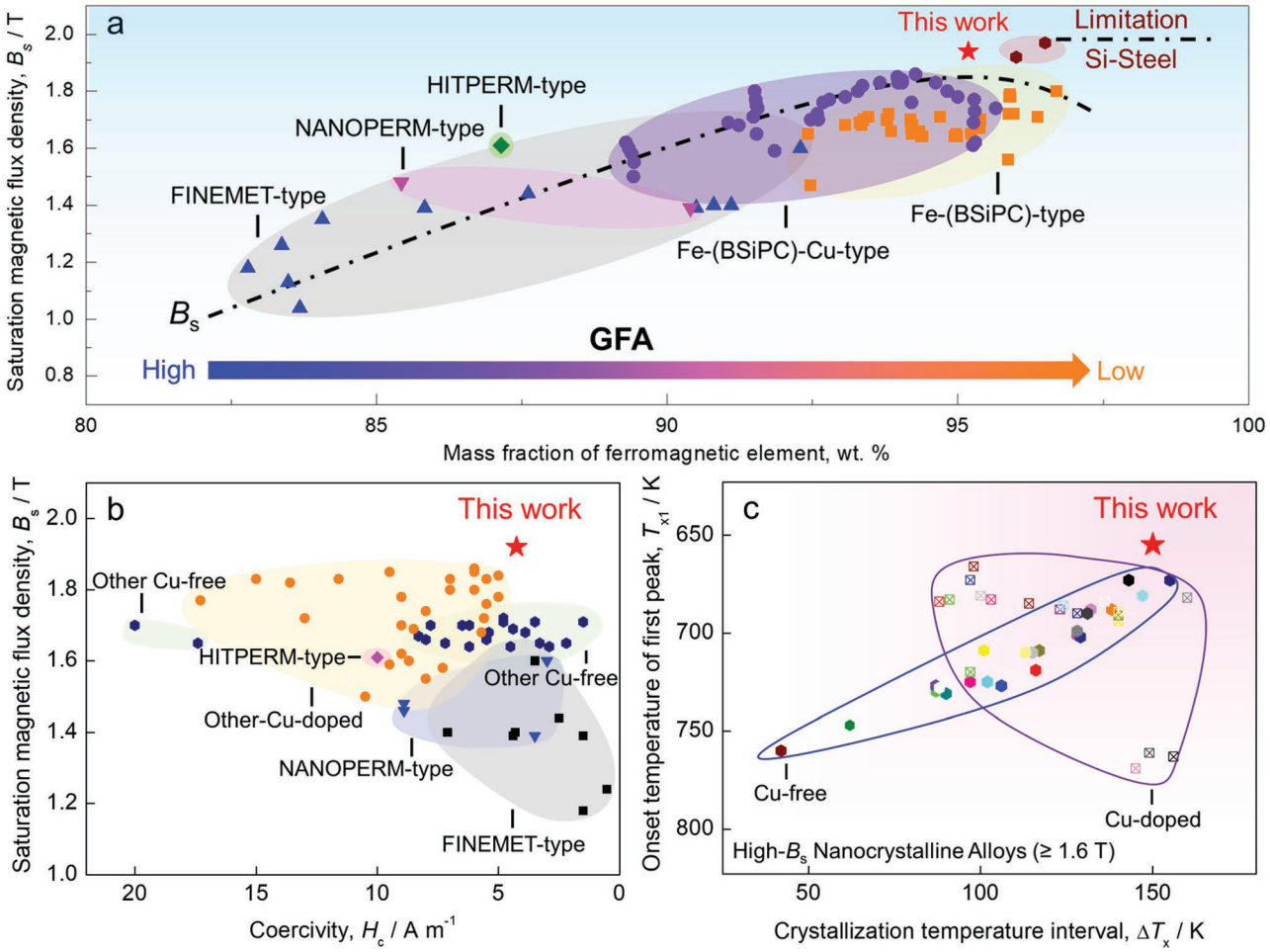

Figure 4. Summary of the excellent soft magnetic properties (e.g., B_s and H_c) and thermal characteristic parameters of typical Fe-based nanocrystalline alloys.[9,11,19,27–31,40–56] a) Variation of B_s and GFA with the mass fraction of ferromagnetic element for FINEMET-type, NANOPERM-type, HITPERM-type, Fe-(BSiPC)-Cu-type, Fe-(BSiPC)-type nanocrystalline alloys, and typical silicon steels. b) Relation between maximum B_s and H_c value for FINEMET-type, NANOPERM-type, HITPERM-type, other Cu-free, and other Cu-doped nanocrystalline alloys.[9,11,19,27–31,40–56] c) Relation between ΔT_x and T_{x1} values for nanocrystalline alloys with high B_s exceeding 1.6 T.[11,27–30,40–47]

In order to elucidate the magnetic structure of $(Fe_{0.8}Co_{0.2})_{85}$ ANT alloy with low H_c, the motion of magnetic domains in samples with different annealing times in varying magnetic fields was observed. Figure S6 (Supporting Information) shows the motion of the magnetic domain of $(Fe_{0.8}Co_{0.2})_{85}$ alloy ribbons with different annealing times observed by magneto-optical Kerr effect (MOKE) microscope. All of the samples exhibit uniaxial anisotropic magnetic domain morphology induced by a longitudinal magnetic field. As magnetic fields parallel to the direction of the ribbons increase, the domain walls travel perpendicular to the direction of the ribbons and eventually disappear (Figure S6a–c, Supporting Information). We then calculated the changes in magnetic fields required for the entire process from the appearance of the domain walls to their disappearance (Figure S6d, Supporting Information). Results show that the magnetic field required by the sample with the lowest coercivity (10 min) has the smallest interval of 5.06 mT, which indicates that the magnetic domain motion of the sample with the annealing time of 10 min is subject to the lowest resistance.

Compared with a traditional MOKE microscope, magnetic domains and domain walls can be observed with higher resolution and clarity by using a magnetic force microscope (MFM).[57,58] Such as the variation of domain wall thickness and pinning field of domain wall can be investigated, which are the crucial parameters affecting the soft magnetic properties of Fe-based AN alloys. However, since the small demagnetized field of soft magnetic materials and the strong stray magnetic field between the MFM cantilever beam and the ribbon surface, the material is likely to be magnetized to saturation without an external magnetic field, it is difficult to directly observe distinct static domains and domain walls of Fe-based AN alloys through MFM, let alone the magnetic domain changes under different external fields. Here, an external magnetic field was attached to the MFM, which is generated by a home-built electromagnet after calibrating with a Hall probe. In addition, we preset the external out-of-plane magnetic field to balance the influence of the cantilever beam, and successfully observed the magnetic domain and the motion of the domain walls (**Figure 5**). All samples were previously demagnetized in the

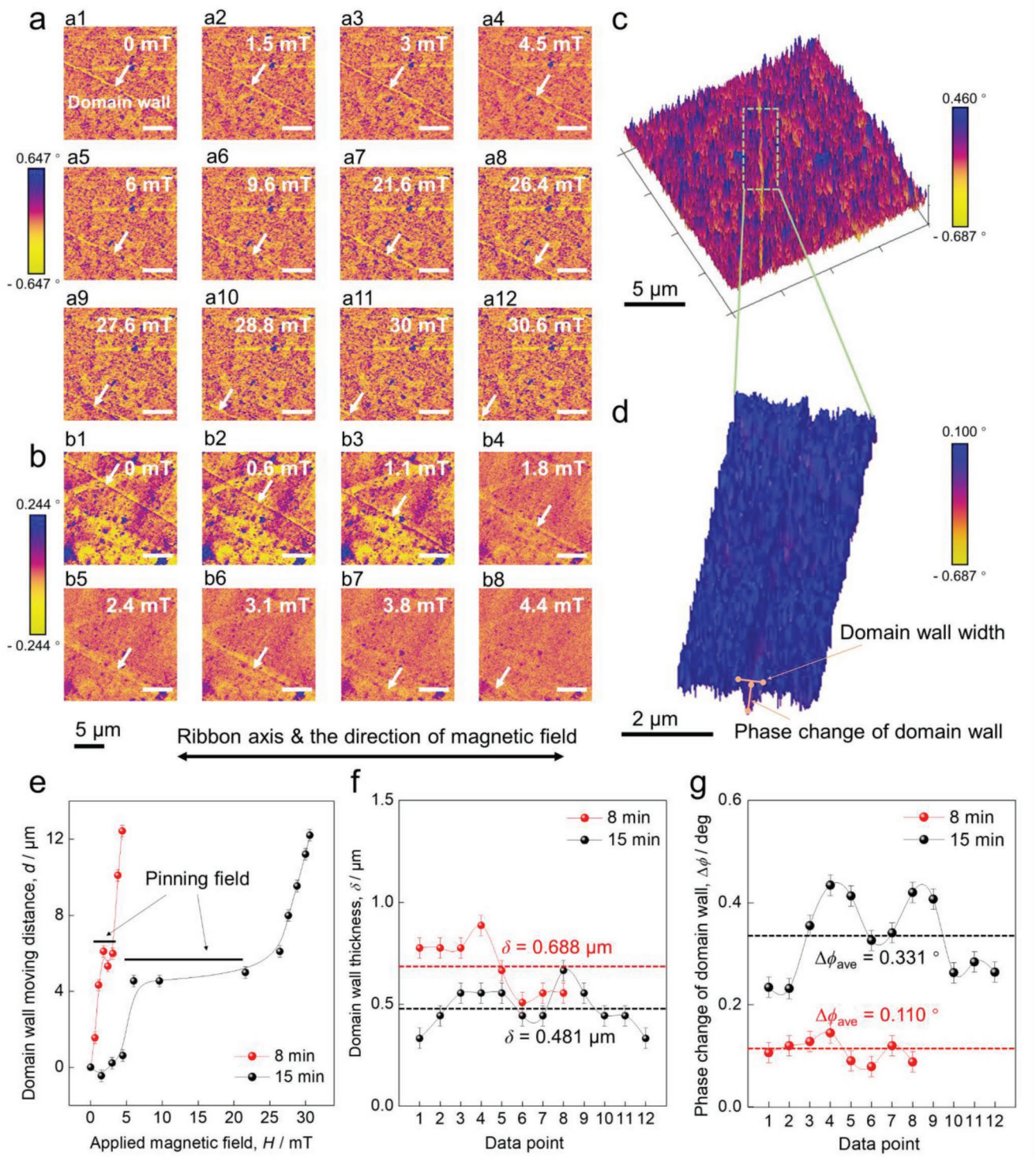

Figure 5. Magnetic domain structures of $(Fe_{0.8}Co_{0.2})_{85}$ alloy ribbons under different annealing times using a magnetic force microscope. Series of 2D-MFM images obtained in the same region of $(Fe_{0.8}Co_{0.2})_{85}$ alloy in varying external magnetic fields with the annealing time of 15 min (a1–a12) and 10 min (b1–b8). c) The 3D-MFM surface topography of demagnetized sample with the annealing time of 15 min. d) Enlarged image of the dotted area in (c). e) The variation of DW moving distance of $(Fe_{0.8}Co_{0.2})_{85}$ alloy under different external magnetic field with the annealing time of 15 and 10 min. f,g) The DW thickness (f) and phase changes (g) of $(Fe_{0.8}Co_{0.2})_{85}$ alloy in varying external magnetic field with the annealing time of 15 and 10 min in all images.

direction parallel to the ribbon axis. Imaging the entire region (20 μm × 20 μm) under an external in-plane magnetic field, two magnetic domains oriented in different directions are separated by DWs. Figure 5a1–a12 show a series of 2D MFM (2D-MFM) images obtained in the same region of $(Fe_{0.8}Co_{0.2})_{85}$ alloy with the annealing time of 15 min (H_c = 12.5 A m^{-1}) when the

in-plane magnetic field parallel to ribbon axis is swept from 0 to 30.6 mT, which is consistent to the MOKE results. The DW in the demagnetized image is tilted and straight in the middle of the image (Figure 5a1). With the increase of the magnetic field, the DW moves down perpendicular to the ribbon axis. Among them, the motion of the DW is hindered from 6 to 21.6 mT, showing a pinning effect. Then the domain monotonous forward moves to the corner of the image with the increase of the external magnetic field to 30.6 mT. During the process, the DW moved ≈12 μm in the direction perpendicular to itself. In the following, we performed the same measurement on $(Fe_{0.8}Co_{0.2})_{85}$ ANT alloy with the annealing time of 10 min (H_c = 4.3 A m^{-1}), recording the whole process of DW moving along ≈12 μm perpendicular to itself, as shown in Figure 5b1–b8. Inspiringly, the sample with low H_c of 4.3 A m^{-1} required an external magnetic field as low as 4.4 mT to complete the whole process. Besides, the motion of the DW is hindered from 1.8 to 3.1 mT, and the DW displays a slight backshift in this range. Through counting the information of each image in Figure 5a,b, the variation of DW moving distance of two samples with the external magnetic field is shown in Figure 5e, reflecting the discrepancy intuitively. Compared with the sample with high H_c of 12.5 A m^{-1}, a lower external magnetic field is required to induce domain motion in the sample with the H_c of 4.3 A m^{-1}. Meanwhile, the pinning effect of DW is also significantly weaker. Then all 2D-MFM images were converted into 3D images. As a typical example, the 3D-MFM surface topography of a demagnetized sample with the annealing time of 15 min (Figure 5a1) is shown in Figure 5c. The region near the DW is then zoomed in to observe its higher-resolution features and details, which are shown in Figure 5d. Subsequently, the DW thickness and phase changes of the two samples in all images were counted and listed in Figure 5f and Figure 5g, respectively. Results show that both the thickness and phase changes of DWs alter slightly with relatively stable values during the intensification of the external magnetic field. The average DW thickness (δ) of the sample annealed for 10 min is larger, while the average phase changes of the DW ($\Delta\phi_{ave}$) are smaller than that of the sample with an annealing time of 15 min.

As amorphous alloys do not possess dislocations or grain boundaries discrepant with crystalline materials, the H_c is mainly dominated by the short-range stress fields generated by quasi-dislocation dipoles, which act as strong pinning sites of magnetic DWs and hinders the motion of magnetic domains.[16,17] When the nanocrystalline process is induced in amorphous alloys, dispersed nanocrystals are precipitated in the amorphous matrix.[9] According to the random anisotropy theory,[8,59] the value of H_c is proportional to the effective anisotropy and inversely proportional to the six powers of the grain size, that is, the small grain size of nanocrystals leads to low effective anisotropy, which in turn reduce H_c of the nanocrystalline alloys. For $(Fe_{0.8}Co_{0.2})_{85}$ ANT alloy developed using this alloy design strategy, an ideal low volume fraction nanocrystalline–amorphous dual-phase structure can be obtained during a suitable nanocrystalline process (annealing at 673 K for 10 min under longitudinal magnetic field) with the H_c as low as 4.3 A m^{-1}. It is believed that such low H_c of high B_s $(Fe_{0.8}Co_{0.2})_{85}$ is the consequence of the combined contribution of the low density of quasi-dislocation dipoles and low effective anisotropy. According to the previous TEM results in Figure 2, the nanocrystals for optimal soft magnetic properties are fine and diffuse precipitated in $(Fe_{0.8}Co_{0.2})_{85}$ ANT alloy. Such small average grain sizes in nanocrystalline alloys are usually lower than the magnetic exchange correlation length, and the effective anisotropy is averaged to a minor value, contributing to the reduction of H_c.[41] The reduced H_c of AN alloys can also be attributed to the pinning effect of the domain wall to reduce spatial fluctuations and simplify domain wall configurations.[60] When the grain size is in the 50–100 nm range, the larger grain size will lead to pinning of the domain walls at grain boundaries. In the optimal annealing process, the grain size of the alloy is small in the range of 10–25 nm, and the pinning effect of grain boundaries on the domain walls is weak.[61] However, when the annealing time of $(Fe_{0.8}Co_{0.2})_{85}$ is extended to 15 min (Figure S4, Supporting Information), the sharp growth of irregular grains also contributes to the increase of the pinning field. In the following, the contribution of quasi-dislocation dipoles and pinning sites of DWs to coercivity (H_c^σ) are mainly considered,[16,17] which are given as:

$$H_c^\sigma = \frac{12G\Delta V}{\sqrt{30F\delta}}\sqrt{\pi\rho_d \ln\left(\frac{\pi L}{2\delta}\right)}\frac{\lambda_s}{J_s} \quad (1)$$

where ρ_d is the density of quasi-dislocation dipoles, G is the shear modulus, ΔV corresponds to the local volume contraction due to the quasi-dislocation dipoles, F is the area of DW, δ is the thickness of DW, L is the width of the domain and J_s is the saturation magnetic polarization. As shown in Figure 5e, the sample annealed for 10 min shows a smaller DW pinning field than that of the sample annealed for 15 min, declaring fewer pinning sites of DW and lower ρ_d. In addition, it can be seen from Figure 5f that the δ of the sample annealed for 10 min is relatively larger. Since ρ_d is positively and δ is negatively correlated with H_c^σ, resulting in a small H_c^σ dominated by quasi-dislocation dipoles of the sample annealed for 10 min. The ribbon thickness of $(Fe_{0.8}Co_{0.2})_{85}$ is uniform during the melt spinning process, with a statistical average of maximum surface gradients, therefore, the H_c due to the surface irregularity is negligible.[18] Therefore, the low effective anisotropy generated by fine and diffused nanocrystals, weak pinning effect of DW caused by the low density of quasi-dislocation dipoles, and uniform ribbon thickness together contribute to the H_c of ultrahigh B_s $(Fe_{0.8}Co_{0.2})_{85}$ ANT alloy as low as 4.3 A m^{-1}.

5. Conclusion

We have proposed an innovative compositional design concept of amorphous–nanocrystalline transition alloy that enables us to construct a microstructure of sparsely dispersed nanocrystals (together with some CLRs precipitated around the nanocrystalline) in an amorphous matrix. Arising from the unique microstructure, the new ANT alloy of $(Fe_{0.8}Co_{0.2})_{85}B_{12}Si_2V_{0.5}Cu_{0.5}$ with a high B_s up to1.94 T and an extra low H_c of 4.3 A m^{-1} was successfully developed. The combination of extraordinary soft magnetic properties is a breakthrough in a general trade-off between B_s and H_c in the soft magnetic material family. The exceptionally high B_s are the result of strong exchange

interactions of local magnetic moments, caused by the combination of suitable ratio of ferromagnetic elements and small sizes of nested nanocrystals and <5 nm-sized CLRs dispersed in the amorphous matrix. In addition, the low H_c benefits from the weak pinning effect of DWs together with the low effective anisotropy caused by this unique microstructure. Such compositional design concept to construct unique microstructure and domain motions allow us to develop more amorphous-based alloys with superior magnetic properties, which may find various applications in modern electronics such as high-speed motor machines, distribution transformers, high-power photovoltaic grid-connected inverters, to name but a few.

6. Experimental Section

Sample Preparation: The alloy ingots were prepared by arc melting the mixture of pure Fe (99.99 wt%), Co (99.95 wt%), B (99.99 wt%), Si (99.999 wt%), V (99.9 wt%), and Cu (99.99 wt%) elements in an argon atmosphere after a high vacuum of 5×10^{-3} Pa. Ribbon samples with a width of 1.5 mm and thickness of 17–30 µm were prepared by single-roller melt spinning with a linear velocity for the copper wheel of 30–40 m s^{-1}. The effectiveness of this GFA evaluating method through preparing ribbons with critical thickness had been proved in the development of other high-B_s AN alloys for the ribbon production.[11,33] The Archimedes method had been used to measure the density of alloy ingot, and more than five tests on each batch of the alloy ingots had been performed. The density value fluctuated between 7.67 and 7.81 g cm^{-3}, which was much smaller than the calculated value of its amorphous state.[62] Taking into account the measurement error, the minimum density value of 7.67 g cm^{-3} was chosen to calculate the B_s value.

Thermal and Structural Characterization: Thermal analysis and amorphous structure of the as-quenched ribbon samples were identified by DSC (Netzsch 404 F3) at a heating rate of 40 K min^{-1} and XRD (Bruker D8 ADVANCE) with the Cu-$K\alpha$ radiation. Magnetic-field-assisted heat treatment was made at 673 K with annealing time ranging from 5 to 15 mins. The annealing equipment we used was a conventional tubular magnetic annealing furnace, which uses resistance wires to preheat the furnace chamber to the target temperature. After stabilizing the temperature, the samples stored in vacuum (less than 10^{-3} Pa) were placed in the specified position of the furnace chamber, and taken out when the annealing time arrived. A longitudinal magnetic field of 1000 Gs was applied throughout the process. The microstructure of annealed alloys was investigated by TEM (JEM F200) with a field-emission gun operated at 300 kV. The TEM samples were prepared by the ion milling method (Gatan Inc., PIPS-M691) under liquid-nitrogen-cooling conditions.

Magnetic Property Tests: Magnetic properties of B_s, H_c, and μ_e were measured by a vibrating sample magnetometer (VSM, Lake Shore 7410) under the maximum applied field of 400 kA m^{-1}, a DC *B*–*H* loop tracer (RIKEN BHS-40) under a field of 800 A m^{-1}, and an impedance analyzer (Agilent 4294A) under the applied field of 1 A m^{-1}, respectively. The temperature dependence of magnetization was measured with a magnetic property measurement system (MPMS, Quantum Design) at a heating rate of 5 K min^{-1}. Magnetic domain motion with the external magnetic field was observed by a MOKE (em-Kerr-highres). Prior to the measurement, a background image was collected as a reference in the AC demagnetized state. The images acquired at different applied fields were enhanced by subtracting the background image using KerrLab software. The magnetic domain model and magnetization process of the ribbon samples were further observed by MFM (Dimension ICON with Nano Scope V controller, Bruker). For the measurements, Si cantilevers coated with a Co film with the normal resonance frequency of 75 kHz and spring constant of 2.8 N m^{-1} (PPP-MFMR, Nanosensors) were used for MFM images. The distance between the tip and sample is maintained at a constant distance of 50 nm. The external magnetic field was generated by a home-built electromagnet after calibrating with a Hall probe, which was parallel to the substrate plane. The photos and structure representation of MFM used in the present work are shown in Figure S7 (Supporting Information). The long-range force interactions between the magnetic probe and samples in MFM were recorded and correlated in the second pass from the shift in phase from the initial driven parameters of the oscillating cantilever, which ultimately manifested as the color contrast in the image.

Supporting Information

Supporting Information is available from the Wiley Online Library or from the author.

Acknowledgements

X.L. and J.Z. contributed equally to this work. This work was supported by the Guangdong Major Project of Basic and Applied Basic Research, China (Grant Nos. 2019B030302010, 2020B1515120092), National Key Research and Development Plan (Grant No. 2018YFA0703603), and the National Natural Science Foundation of China (Grant Nos. 52192601, 52192602, 52101191, 11790291, and 61888102). The authors would like to thank D.Z. in the Materials Growth and Characterization Center of Songshan Lake Materials Laboratory for the MFM testing.

Conflict of Interest

The authors declare no conflict of interest.

Data Availability Statement

The data that support the findings of this study are available from the corresponding author upon reasonable request.

Keywords

coercivity, magnetic domains, nanocrystalline alloys, saturation magnetic flux density, transitional microstructure

Received: June 28, 2022
Revised: August 24, 2022
Published online:

[1] J. M. Silveyra, E. Ferrara, D. L. Huber, T. C. Monson, *Science* **2018**, *362*, eaao0195.
[2] E. A. Perigo, B. Weidenfeller, P. Kollár, J. Füzer, *Appl. Phys. Rev.* **2018**, *5*, 031301.
[3] O. Gutfleisch, M. A. Willard, E. Brück, C. H. Chen, S. G. Sankar, J. P. Liu, *Adv. Mater.* **2011**, *23*, 821.
[4] M. E. McHenry, M. A. Willard, D. E. Laughlin, *Prog. Mater. Sci.* **1999**, *44*, 291.
[5] M. E. McHenry, D. E. Laughlin, *Acta Mater.* **2000**, *48*, 223.
[6] B. D. Cullity, C. D. Graham, John Wiley & Sons **2011**.
[7] S. Kasai, M. Namikawa, T. Hiratani, *JFE Tech. Rep.* **2016**, *21*, 12.
[8] G. Herzer, *Acta Mater.* **2013**, *61*, 718.
[9] Y. Yoshizawa, S. Oguma, K. Yamauchi, *J. Appl. Phys.* **1988**, *64*, 6044.
[10] M. Ohta, R. Hasegawa, *IEEE Trans. Magn.* **2016**, *53*, 2000205.

[11] H. Li, A. D. Wang, T. Liu, P. B. Chen, A. N. He, Q. Li, J. H. Luan, C. T. Liu, *Mater. Today* **2021**, *42*, 49.
[12] R. Parsons, Z. Li, K. Suzuki, *J. Magn. Magn. Mater.* **2019**, *485*, 180.
[13] R. Parsons, B. Zang, K. Onodera, H. Kishimoto, T. Shoji, A. Kato, K. Suzuki, *J. Magn. Magn. Mater.* **2019**, *476*, 142.
[14] R. Hasegawa, CRC Press, Boca Raton, FL **1983**.
[15] M. Srinivas, B. Majumdar, S. Bysakh, M. M. Raja, D. Akhtar, *J. Alloy. Compd.* **2014**, *583*, 427.
[16] H. Kronmüller, *J. Appl. Phys.* **1981**, *52*, 1859.
[17] H. Kronmüller, *J. Magn. Magn. Mater.* **1981**, *24*, 159.
[18] T. Bitoh, A. Makino, A. Inoue, *Mater. Trans.* **2004**, *45*, 1219.
[19] M. Ohta, Y. Yoshizawa, *J. Phys. D: Appl. Phys.* **2011**, *44*, 064004.
[20] M. Yu, Y. Kakehashi, *Phys. Rev. B* **1994**, *49*, 15723.
[21] A. L. Greer, *Nature* **1993**, *366*, 303.
[22] B. Zang, R. Parsons, K. Onodera, H. Kishimoto, A. Kato, A. C. Y. Liu, K. Suzuki, *Scr. Mater.* **2017**, *132*, 68.
[23] K. Suzuki, R. Parsons, B. Zang, K. Onodera, H. Kishimoto, T. Shoji, A. Kato, *J. Alloy. Compd.* **2018**, *735*, 613.
[24] L. Xie, T. Liu, A. N. He, Q. Li, Z. Gao, A. Wang, C. Chang, X. Wang, C. T. Liu, *J. Mater. Sci.* **2018**, *53*, 1437.
[25] M. Mitera, M. Naka, T. Masumoto, N. Kazama, K. Watanabe, *Phys. Status Solidi A* **1978**, *49*, K163.
[26] A. Williams, V. Moruzzi, A. Malozemoff, K. Terakura, *IEEE Trans. Magn.* **1983**, *19*, 1983.
[27] L. Hou, X. Fan, Q. Wang, W. Yang, B. Shen, *J. Mater. Sci. Technol.* **2019**, *35*, 1655.
[28] Z. Shi, R. Li, T. Zhang, *J. Alloy. Compd.* **2019**, *778*, 302.
[29] H. Zheng, L. Zhu, S. S. Jiang, Y. G. Wang, S. N. Liu, S. Lan, F. G. Chen, *J. Alloy. Compd.* **2020**, *816*, 152549.
[30] L. Hou, M. Li, C. Jiang, X. Fan, Q. Luo, S. Chen, P. Song, W. Li, *J. Alloy. Compd.* **2021**, *853*, 157071.
[31] A. Takeuchi, A. Inoue, *Mater. Trans.* **2005**, *46*, 2817.
[32] C. Zhao, A. Wang, A. He, C. Chang, C.-T. Liu, *Sci. China Mater.* **2021**, *64*, 1813.
[33] J. Wang, P. Jiang, F. Yuan, X. Wu, *Nat. Commun.* **2022**, *13*, 1021.
[34] N. Kuwano, N. Chiwata, K. Oki, *Bull. Mater. Sci.* **1999**, *22*, 697.
[35] G. V. Tendeloo, S. Amelinckx, *Phase Transitions* **1998**, *67*, 101.
[36] Y. Xie, S. Sohn, M. Wang, H. Xin, Y. Jung, M. D. Shattuck, C. S. O'Hern, J. Schroers, J. J. Cha, *Nat. Commun.* **2019**, *10*, 915.
[37] J. Dai, Y. G. Wang, L. Yang, G. T. Xia, Q. S. Zeng, H. B. Lou, *Scr. Mater.* **2017**, *127*, 88.
[38] X. Tong, Y. Zhang, Y. Wang, X. Liang, K. Zhang, F. Zhang, Y. Cai, H. Ke, G. Wang, J. Shen, A. Makino, W. Wang, *J. Mater. Sci. Technol.* **2022**, *96*, 233.
[39] Q. Luo, D. Li, M. Cai, S. Di, Z. Zhang, Q. Zeng, Q. Wang, B. Shen, *J. Mater. Sci. Technol.* **2022**, *116*, 72.
[40] C. Wu, H. Chen, H. Lv, M. Yan, *J. Alloy. Compd.* **2016**, *673*, 278.
[41] K. Suzuki, A. Makino, A. Inoue, T. Masumoto, *J. Appl. Phys.* **1991**, *70*, 6232.
[42] M. A. Willard, D. E. Laughlin, M. E. McHenry, D. Thoma, K. Sickafus, J. O. Cross, V. G. Harris, *J. Appl. Phys.* **1998**, *84*, 6773.
[43] X. D. Fan, H. Men, A. B. Ma, B. L. Shen, *J. Magn. Magn. Mater.* **2013**, *326*, 22.
[44] F. F. Marzo, A. R. Pierna, A. Altube, *J. Non-Cryst. Solids* **2001**, *287*, 349.
[45] F. Wan, A. He, J. Zhang, J. Song, A. Wang, C. Chang, X. Wang, *J. Electron. Mater.* **2016**, *45*, 4913.
[46] E. N. Zanaeva, A. I. Bazlov, D. A. Milkova, A. Y. Churyumov, A. Inoue, N. Y. Tabachkova, F. Wang, F. L. Kong, S. L. Zhu, *J. Non-Cryst. Solids* **2019**, *526*, 119702.
[47] Y. L. Li, Z. X. Dou, X. M. Chen, K. Lv, F. S. Li, X. D. Hui, *J. Alloy. Compd.* **2020**, *844*, 155767.
[48] A. Urata, M. Yamaki, M. Takahashi, K. Okamoto, H. Matsumoto, S. Yoshida, A. Makino, *J. Appl. Phys.* **2012**, *111*, 07A335.
[49] A. Makino, H. Men, K. Yubuta, T. Kubota, *J. Appl. Phys.* **2009**, *105*, 013922.
[50] T. Liu, F. Kong, L. Xie, A. Wang, C. Chang, X. Wang, C.-T. Liu, *J. Magn. Magn. Mater.* **2017**, *441*, 174.
[51] F. G. Chen, Y. G. Wang, *J. Alloy. Compd.* **2014**, *584*, 377.
[52] Y. Jin, X. Fan, H. Men, X. Liu, B. Shen, *Sci. China Technol. Sci.* **2012**, *55*, 3419.
[53] M. Ohta, Y. Yoshizawa, *Appl. Phys. Lett.* **2007**, *91*, 062517.
[54] L. Shi, K. Yao, *Mater. Des.* **2020**, *189*, 108511.
[55] F. L. Kong, C. T. Chang, A. Inoue, E. S. Shalaan, F. Al-Marzouki, *J. Alloy. Compd.* **2014**, *615*, 163.
[56] Y. Han, F. Kong, C. Chang, S. Zhu, A. Inoue, E.-S. Shalaan, F. Al-Marzouki, *J. Mater. Res.* **2015**, *30*, 547.
[57] C. T. Hsieh, J. Q. Liu, J. T. Lue, *Appl. Surf. Sci.* **2005**, *252*, 1899.
[58] O. Kazakova, R. Puttock, C. Barton, H. Corte-León, M. Jaafar, V. Neu, A. Asenjo, *J. Appl. Phys.* **2019**, *125*, 060901.
[59] G. Herzer, *J. Magn. Magn. Mater.* **2005**, *294*, 99.
[60] G. Herzer, *J. Magn. Magn. Mater.* **1992**, *112*, 258.
[61] M. A. Willard, *Handbook of Magnetic Materials* **2013**, *21*, 173.
[62] R. Parsons, K. Ono, Z. Li, H. Kishimoto, T. Shoji, A. Kato, M. R. Hill, K. Suzuki, *J. Alloy. Compd.* **2021**, *859*, 157845.